Supplementary Information for

Macroscopic Assembled Graphene for Silicon Mid-Infrared Photodetectors

Li Peng[1,10], Sichao Du[2,10], Lixiang Liu[2,10], Srikrishna Chanakya Bodepudi[2], Lingfei Li[2], Wei Liu[2], Xin Cong[3], Runchen Lai[4], Wenzhang Fang[1], Xiaoxue Cao[1,2], Xinyu Liu[2], Muhammad Abid[2], Jianhang Lv[2], Junxue Liu[4], Shengye Jin[4], Kaifeng Wu[4], Qiaohui Zhou[5], Haiming Zhu[5], Miao-Ling Lin[3], Ping-Heng Tan[3], Qihua Xiong[6], Xiaomu Wang[7], Weida Hu[8], Xiangfeng Duan[9], Bin Yu[2], Wenyan Yin[2], Zhen Xu[1], Yang Xu[2*], Chao Gao[1*]

[1]MOE Key Laboratory of Macromolecular Synthesis and Functionalization, Department of Polymer Science and Engineering, Zhejiang University, Hangzhou 310027, China.

[2]Colleges of ISEE and Microelectronics, State Key Laboratories of Modern Optical Instrumentation and Silicon Materials, Hangzhou Global Scientific and Technological Innovation Center, ZJU-UIUC Joint Institute, Zhejiang University, Hangzhou 310027, China

[3]State Key Laboratory of Superlattices and Microstructures, Institute of Semiconductors, Chinese Academy of Sciences, Beijing 100083, China

[4]State Key Laboratory of Molecular Reaction Dynamics and Dynamics, Dalian Institute of Chemical Physics, Chinese Academy of Sciences, Dalian 116023, China

[5]Department of Chemistry, Zhejiang University, Hangzhou 310027, China

[6]Division of Physics and Applied Physics, School of Physical and Mathematical Sciences, Nanyang Technological University, Singapore 637371, Singapore

[7]National Laboratory of Solid State Microstructures, Collaborative Innovation Center of Advanced Microstructure, School of Electronic Science and Engineering, Nanjing University, Nanjing 210093, China

[8]National Laboratory for Infrared Physics, Shanghai Institute of Technical Physics, Chinese Academy of Sciences, Shanghai 200083, China

[9]Department of Chemistry and Biochemistry, California Nanosystems Institute, University of California, Los Angeles 90095, USA

[10]These authors contributed equally: Li Peng, Sichao Du, Lixiang Liu

*e-mail: yangxu-isee@zju.edu.cn; chaogao@zju.edu.cn.

Supplementary Note 1. The structural characterizations of MAG.

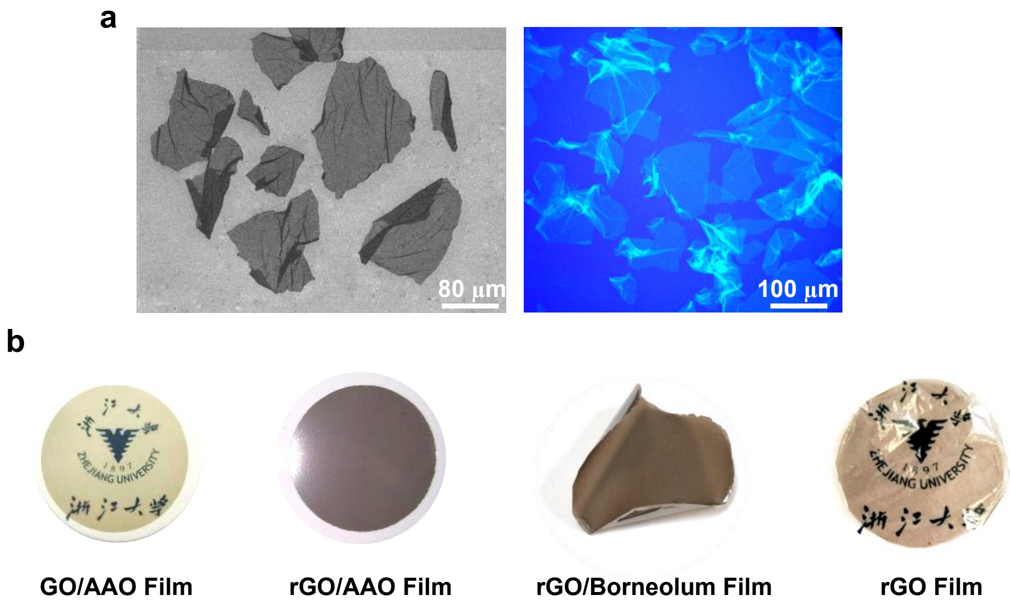

Figure S1 | Sample photos in the MAG preparation process. a, SEM and optical images of GO sheets with an average size of 100 μm on a silicon wafer. **b,** Photos of GO/AAO, rGO/AAO, rGO/borneolum, rGO, and MAG films.

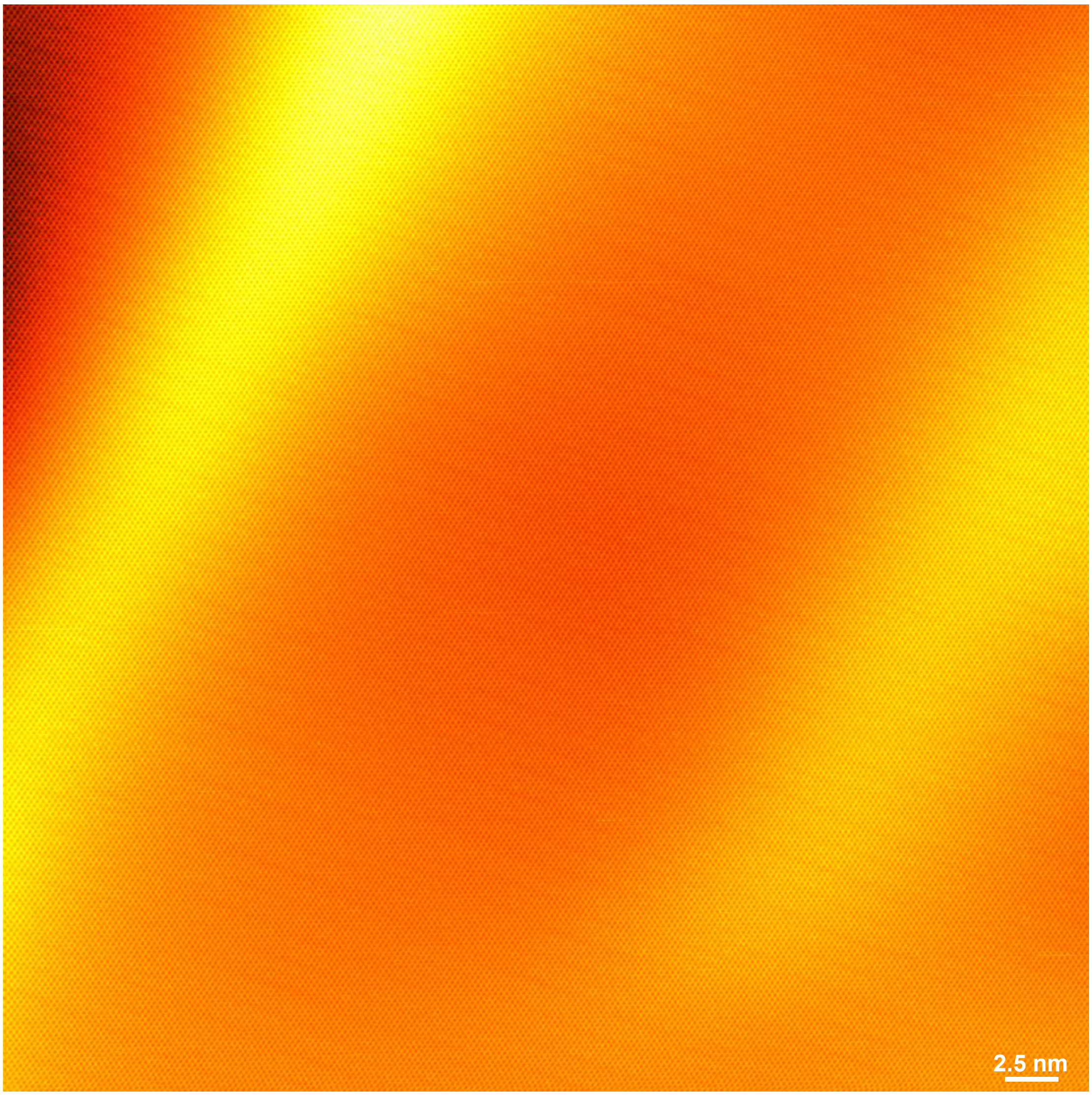

Figure S2 | In-plane structure of MAG. The STM image of the MAG surface at a 50-nm scale**.**

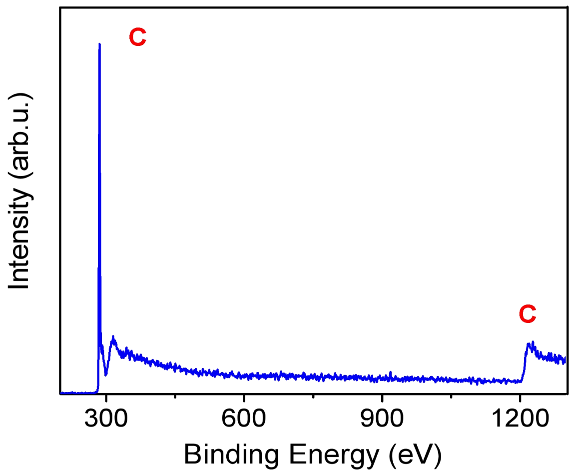

Figure S3 | X-ray Photoelectron Spectroscopy (XPS) spectrum of MAG with no detectable signal of oxygen element.

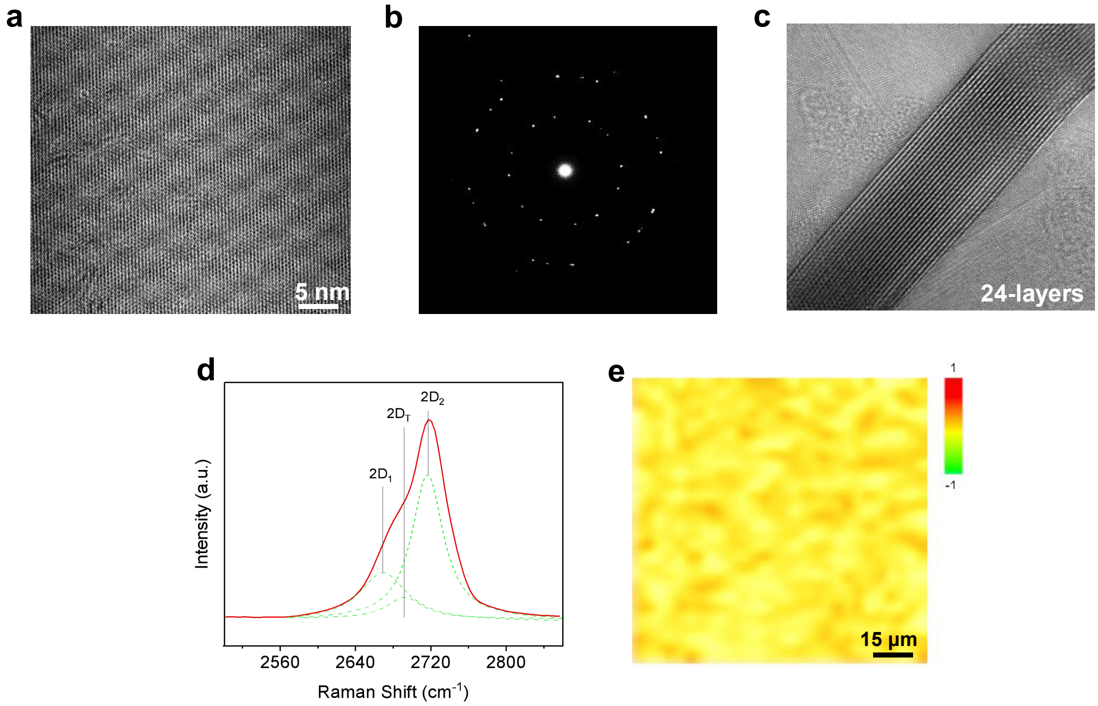

Figure S4 | Stacking structure characterization of MAG. a-c, HR-TEM topographic image of MAG (24 layers) with regular moiré pattern, 4-set of electron diffraction spots, and corresponding cross-section image. **d,** The fitted 2D band by AB stacking structure ($2D_1$ and $2D_2$) and turbostratic structure ($2D_T$)[1]. **e,** Map of the fraction of AB stacking order from the fitted 2D band with the value of $I(2D_T)/(I(2D_2) + I(2D_T))$ in the range of 0.1-0.07.

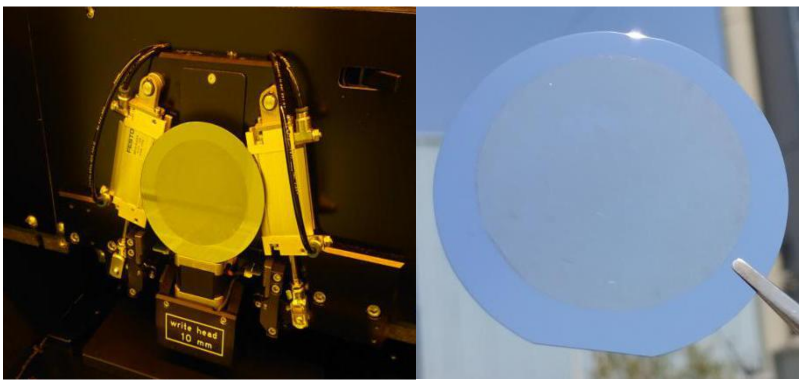

Figure S5 | MAG/Si wafer in and outside the cleanroom.

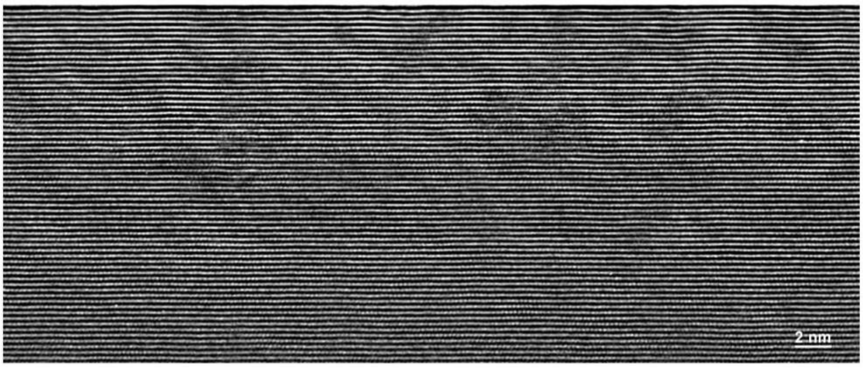

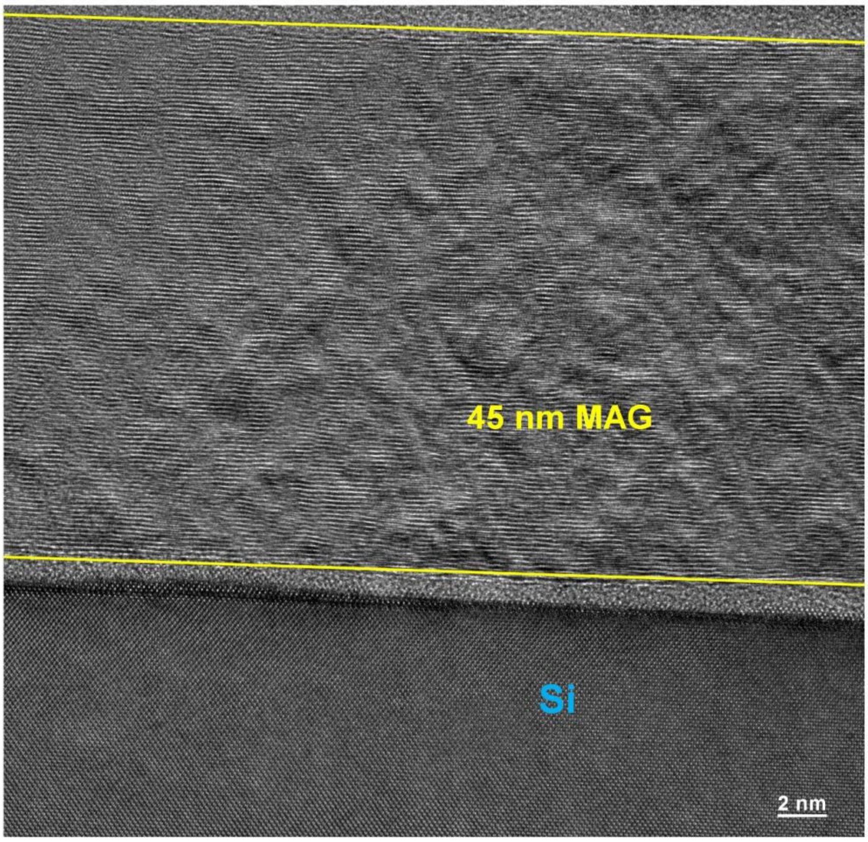

Figure S6 | HR-TEM images of MAG (up) and MAG/Si (down) cross-section.

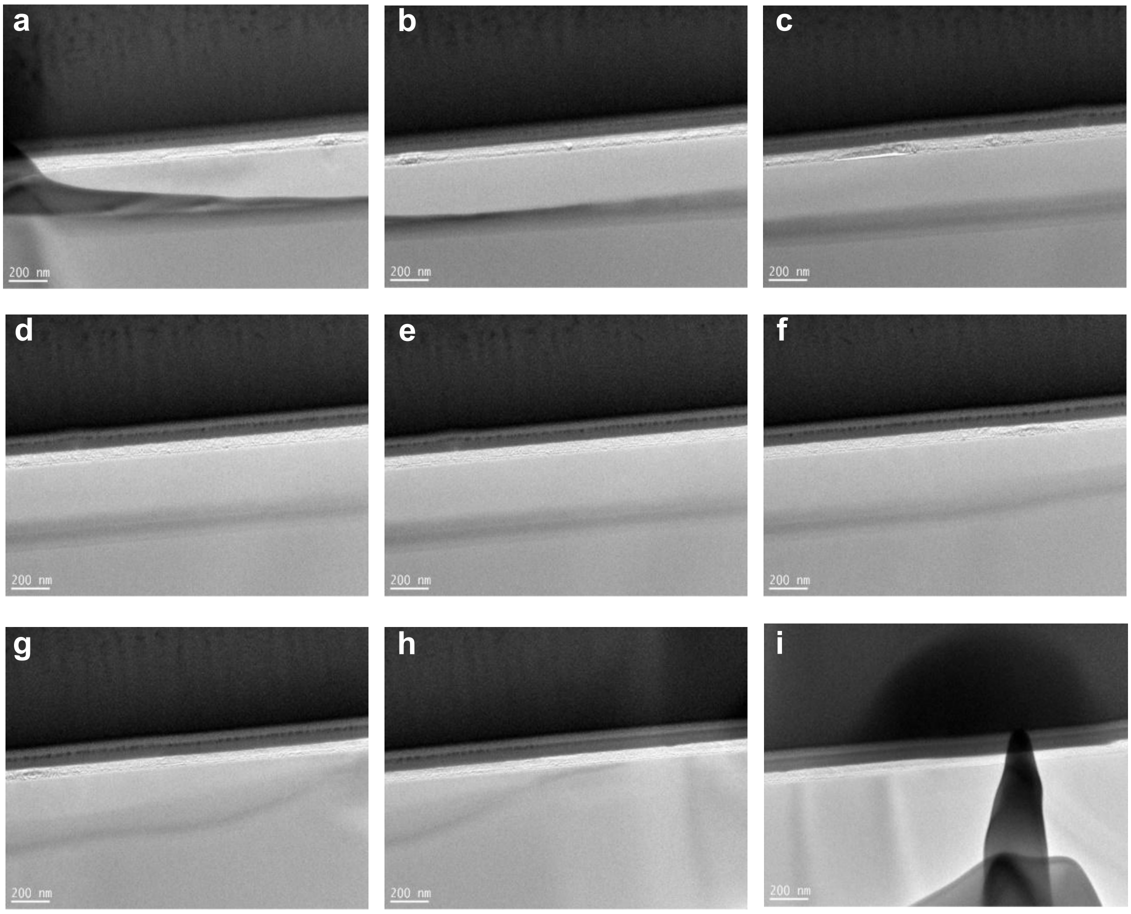

Figure S7 | Continuous cross-sectional TEM images of MAG with a thickness of 45 nm on the silicon substrate.

The 2800°C annealing process drives a rearrangement of the stacking order of MAG form turbostratic structure to AB stacking structure. While the exact mechanism of this transformation is unclear, it seems that the localized structural adjustment roles. At regions of thermodynamic instability such as overlapping grain-boundaries or basal plane defects, there could be a transformation to an AB stacked structure caused by the self-diffusion of carbon atoms. Given the polycrystalline graphene used, a stacked structure might be expected to be almost everywhere turbostratic, but the high-temperature treatment drives the formation of regions of AB-stacked layers, but not a complete transformation to AB graphite. A low interlayer spacing of 3.36 Å was observed by GI-WAXS and HR-TEM, similar to that of HOPG. The high-temperature treatment at 2800 °C has shifted the 2D peak position from 2700 cm^{-1} (turbostratic structure) to 2720 cm^{-1} (graphite structure), suggesting a strong interlayer coupling between the stacked layers. We believe such stacking approaches could generate significant interest in making "synthetic crystals" of other 2D material superlattices that are unobtainable by standard synthesis methods.

Supplementary Note 2. The work function of MAGs with different thicknesses.

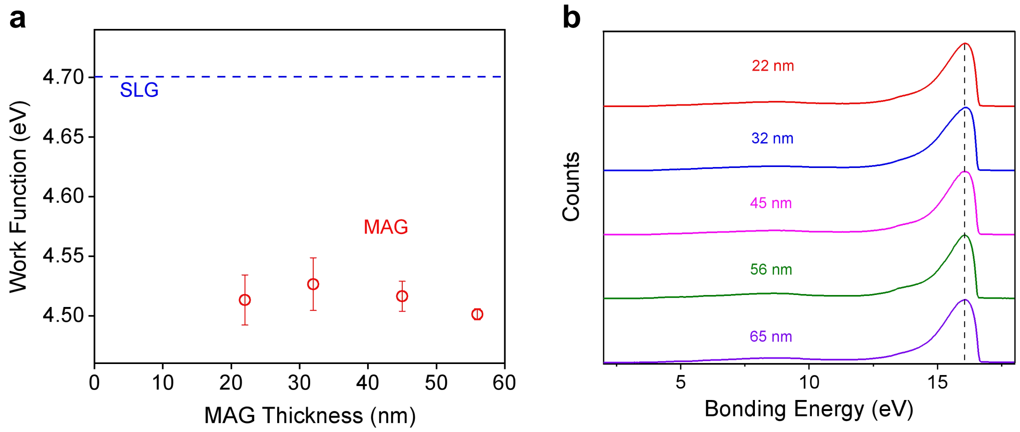

Figure S8 | Work function characterization of MAG. a, The work function measured by the Kelvin probe force microscopy (KPFM). **b,** The ultraviolet photoelectron spectra (UPS) of MAG with different thicknesses.

Table S1 | The datasheet of work function measured by KPFM of HOPG, CVD-MLG, and MAG with different thicknesses.

	HOPG		CVD-MLG		22 nm MAG		32 nm MAG		45 nm MAG		56 nm MAG	
	Mean WF (mV)	Std	Mean WF (mV)	Std	Mean WF (mV)	Std	Mean WF (mV)	Std	Mean WF (mV)	Std	Mean WF (mV)	Std
1	-58.8	7.5	154.7	4.1	-62.9	4.3	-44.5	3.8	-28.9	3.6	-55.9	4.4
2			140.2	4	-61	4.5	-52.4	4	-45.7	3.8	-54.1	4
3					-17.9	4.1	-2.1	4.2	-36.9	4	-62.8	4
4					-40.6	4.2	-30.2	4.1	-58.2	3.8		

The work function is calculated:[Mean WF(Xnm) - Mean WF(HOPG)]/1000 + 4.5.

Supplementary Note 3. The optical properties of MAG/Si.

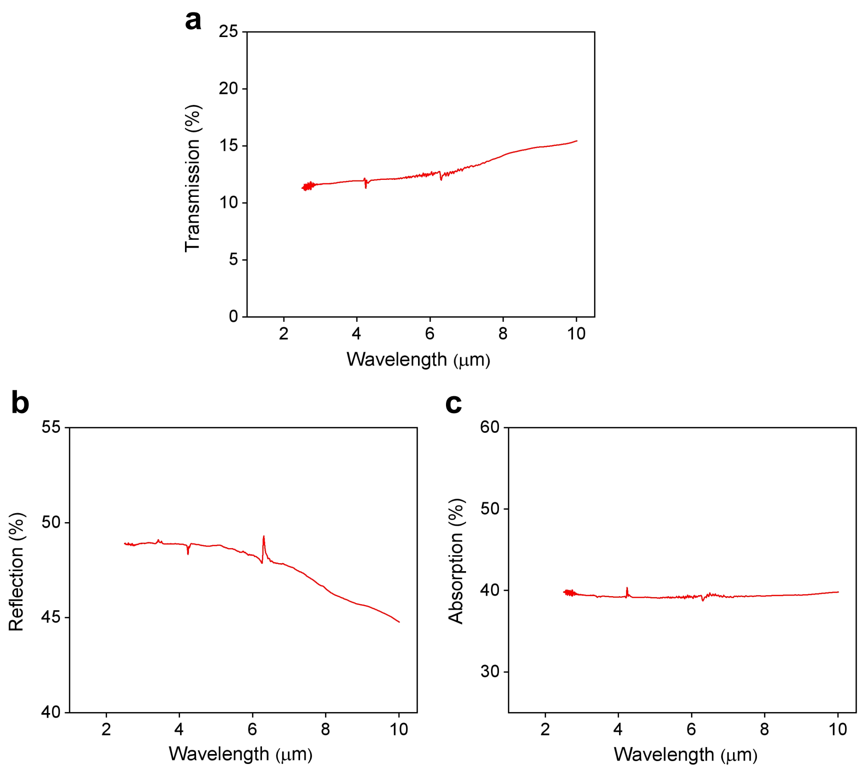

Figure S9 | FTIR characterization of MAG/Si. a-c, Transmission (**a**), reflection (**b**), and absorption (**c**) spectra of MAG (45 nm).

Supplementary Note 4. The SNR of MAG/Si.

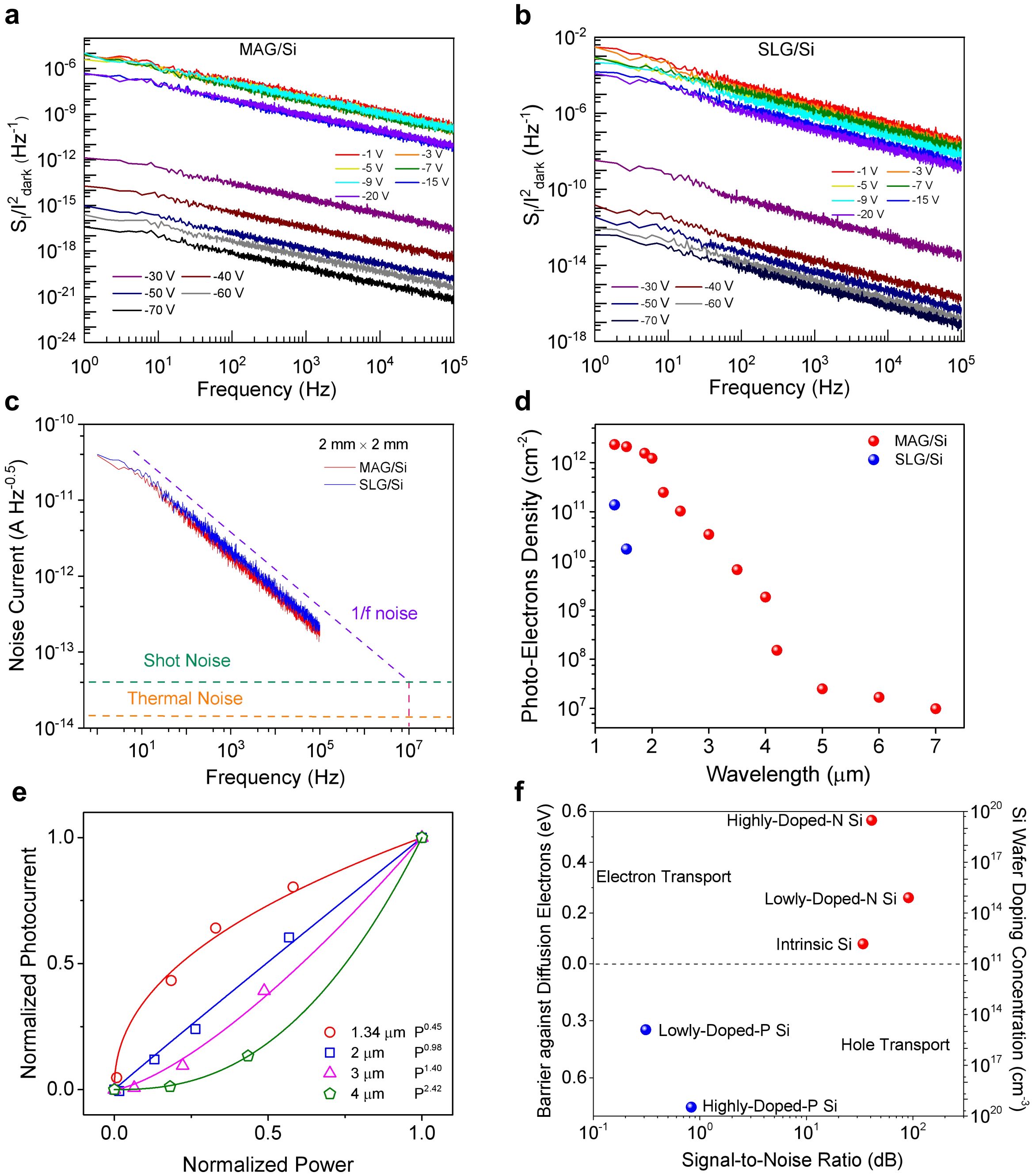

Figure S10 | The SNR of MAG/Si. a-b, The NSD of MAG/Si and SLG/Si as a function of frequency at different bias voltage[2]. **c**, The noise current (at -1 V) of MAG/Si and SLG/Si as a function of frequency. **d**, The photo-electrons density of MAG/Si and SLG/Si as a function of incident laser wavelength at a fixed irradiance of 50 mW mm^{-2}. **e**, The normalized photocurrent of MAG/Si as a function of normalized illumination power from 1.34-4 μm wavelength. **f**, The SNR of MAG/Si with different doping types of silicon substrates[3].

Since the SLG is exposed to traps and disorders on both sides of its surfaces, electrons captured or emitted back to the channel are more pronounced, resulting in a stronger carrier number fluctuation. In contrast, the volume contribution becomes dominant in MAG, where the noise is no longer a surface phenomenon. The NSD $S(f)/I^2_{dark}$ in MAG/Si is nearly identical to that of SLG/Si under low bias voltage, indicating that the atomic-scale interfacial contact of MAG with Si same as that of SLG with silicon (Fig. 2f and Fig. S10a-b)[4]. As the number of stacked graphene layers increases, the percentage of carrier number fluctuation from the surface effect (traps and disorders comparing to the internal volume part) is smaller. At larger bias voltage, $S(f)/I^2_{dark}$ in MAG/Si is smaller than that of SLG/Si, suggesting a higher SNR during avalanche can be achieved in MAG/Si. As the number of stacked graphene layers increases, the Fermi level of MAG is more difficult to be electrical tuned, leading to a slight change of SBH thus the NSD $S(f)/I^2_{dark}$[5]. The photo-excited charge-carriers density was extracted by measuring the transit electrical signal of the devices corresponding to each laser pulse. The MAG/Si shows measurable signals in the wavelength range from 1.34 μm to 7 μm, while the SLG/Si only has measured photoresponse at 1.34 μm and 1.55 μm. Direct single-layer-graphene internal photoemission over a Schottky barrier has been previously studied. The weak hot-electron interaction and the small number of photo-excited electrons results in a photoresponse only at near-infrared (1.3-1.6 μm). Fig. S10c-d exhibits the noise current as a function of frequency, where both of the MAG/Si and SLG/Si have 10^{-11} amperes noise current level at 100 kHz corresponding to the laser repetition rate. The flicker noise, dominating noise source in MAG/Si, can be described by the Hooge relation: $\frac{S_I}{I^2} = \frac{\alpha_H}{Nf}$, where S_I is the noise spectral density and α_H is the Hooge parameter[2]. The white noise: shot ($\overline{i_{shot}^2} = 2eI\Delta f$) and thermal ($\overline{i_{thermal}^2} = \frac{4kT\Delta f}{R}$) noise floor of MAG/Si are 9×10^{-13} amperes and 1×10^{-13} amperes, respectively, indicating that the bandwidth of MAG/Si photodiode goes up to 10 MHz ($f_C = \frac{1}{2\pi R_S C_j}$). Beyond λ = 1.55 μm, the noise current 10^{-11} amperes corresponding to a 10^4 cm^{-2} charge-carriers density, suggesting the MAG/Si enhanced 2 to 8 orders of the photoresponse compared with that of single-layer graphene in the same wavelength range.

Table S2 | The state-of-the-art based graphene-silicon IR photodetectors at room temperature.

Structure	Type	λ (μm)	R (A/W) @λ (μm)	τ (s) @ λ (μm)	D* (Jones) @ λ (μm)
MAG/n-Si	**Schottky**	**1-10**	**10^{-1} @ 4; 10^{-7} @ 10**	**10^{-8} @ 4**	**10^{8}@4 10^{6}@10**
Gr-nanowall/Au/n-Si[5]	Schottky	1.55-3.5	10^{-1} @ 1.55; 10^{-7} @ 3.5	10^{-4} @ 1.55	1.4×10^{10} @1.5
SLG/p-Si[6]	Schottky	1-2	1.6×10^{-4} @ 2	10^{-3} @ 2	/
SLG/Si-QDs/n-Si[7]	Schottky	1-1.87	10^{-1} @ 1.87	10^{-5} @ 1.34	10^{11} @1.87
Gr-film/n-Si[8]	Schottky	1.55	5.2×10^{-2} @ 1.55	10^{-3} @ 1.55	1.4×10^{10} @1.55
Cu/p-Si[9]	Microcavity	1.55	6.3×10^{-5} @ 1.55	10^{-9} @ 1.55	/
Cu/p-Si[10]	Microcavity	1.55	10^{-6} @ 1.55	10^{-9} @ 1.55	/
SLG/p-Si[11]	Microcavity	1.55	2×10^{-2} @ 1.55	10^{-9} @ 1.55	5.1×10^{7} @1.55
$NiSi_2$/Si[12]	Waveguide	1.52-1.62	4.6×10^{-3} @ 1.52; 4.5×10^{-3} @ 1.62	10^{-10} @ 1.55	/
Cu/p-Si[13]	Waveguide	1.52-1.62	8×10^{-5} @ 1.55	10^{-9} @ 1.55	/
SLG/n-Si[14]	Photoconductive	1.55	10^{0} @ 1.55	10^{-6} @ 1.55	10^{8} @1.55
Al/p-Si/Cu[15]	MSM	1.55	4.5×10^{-3} @ 1.55	10^{-9} @ 1.55	/
Si/Ni_2Si/Si[16]	p-n	1.52-1.62	1.2×10^{-2} @ 1.52; 3×10^{-2} @ 1.59	10^{-10} @ 1.55	/

Supplementary Note 5. The photoresponse studies of MAG/Si.

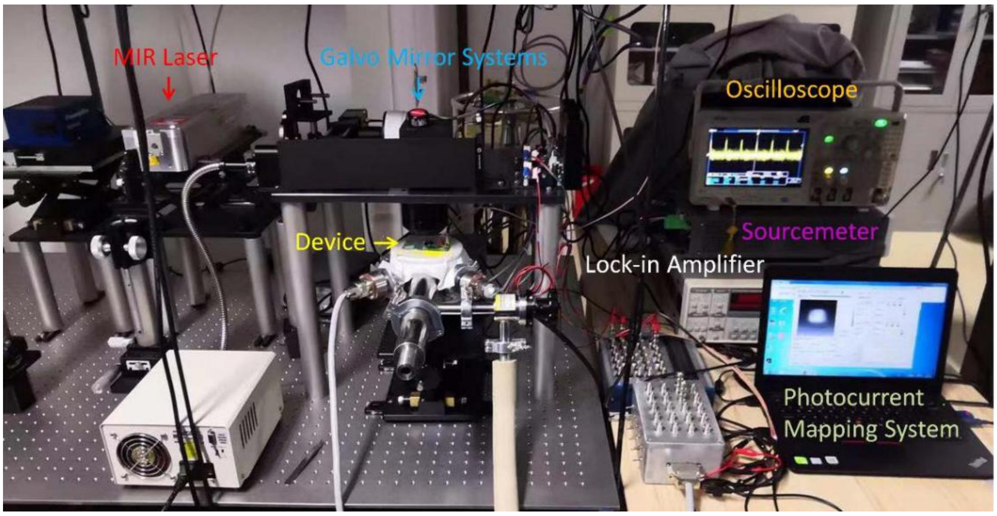

Figure S11 | The MIR photoresponse measurements setup. The photoresponse was measured using lock-in and current amplifiers Stanford SR830 and SR560. A Fabry–Perot quantum cascade laser (Monolux-90, Pranalytica.Inc.) was used as the light source with a scanning photocurrent microscope. The laser beams were focused by a reflection objective. The direct-current electrical characterizations were performed using a Keithley 2636A dual-channel digital source meter. The transient response was measured by a 1 GHz bandwidth oscilloscope[17].

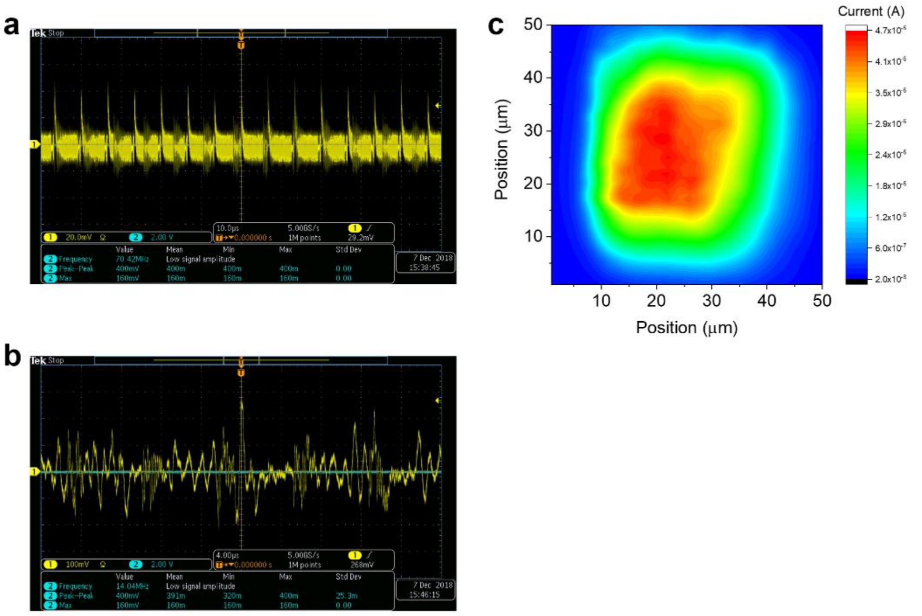

Figure S12 | The MIR photoresponse comparison of MAG/Si and SLG/Si. a-b, The oscilloscope view of transit photoresponse of MAG/Si and SLG/Si under 4 μm laser illumination at 1 mW mm^{-2}. The MAG/Si shows periodic photovoltages corresponding to the laser pulses, while the SLG/Si shows random noise. **c,** The top-view of 2D photocurrent mapping of MAG/Si.

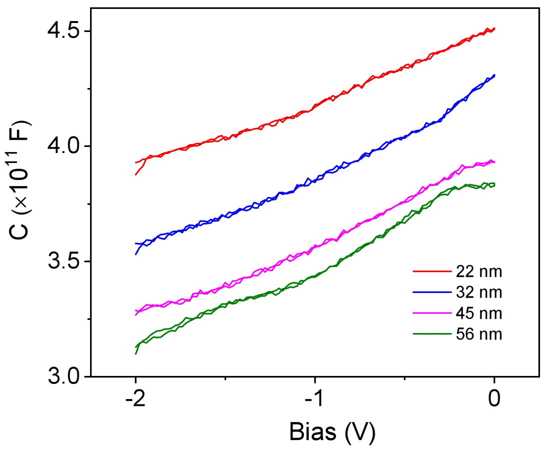

Figure S13 | The capacitance of MAG/Si with different MAG thicknesses under dual-sweep measurement mode.

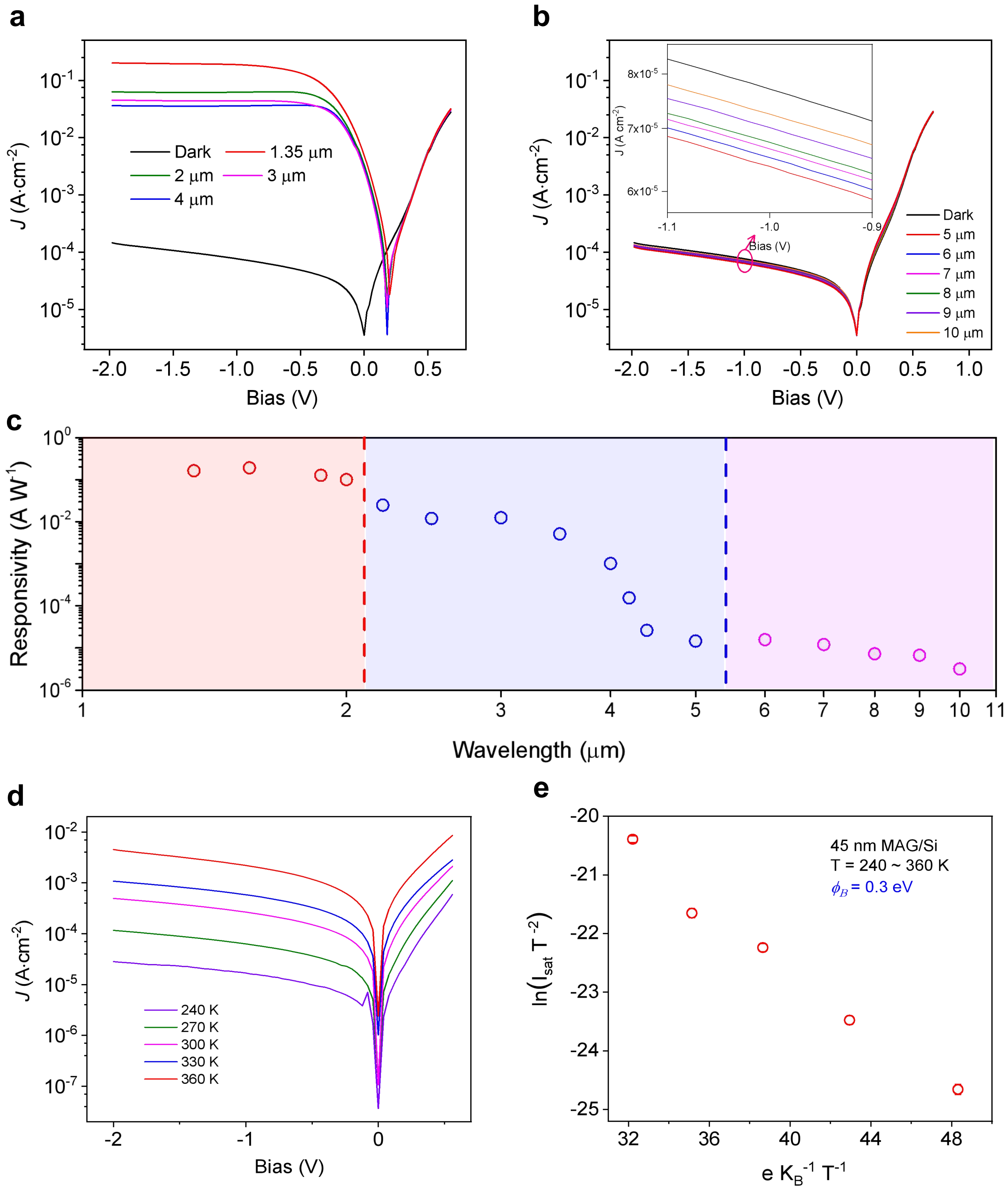

Figure S14 | The *I-V* characterization of MAG/Si. a-b, The *I-V* curves of MAG/Si at incident laser wavelength 1.35-10 μm with a fixed irradiance of 50 mW mm^{-2}. **c,** The corresponding photo-responsivity as a function of the laser wavelength. **d,** The *I-V* curves of MAG/Si under dark at different temperatures from 240-360 K. **e,** Extracted SBH from **d**.

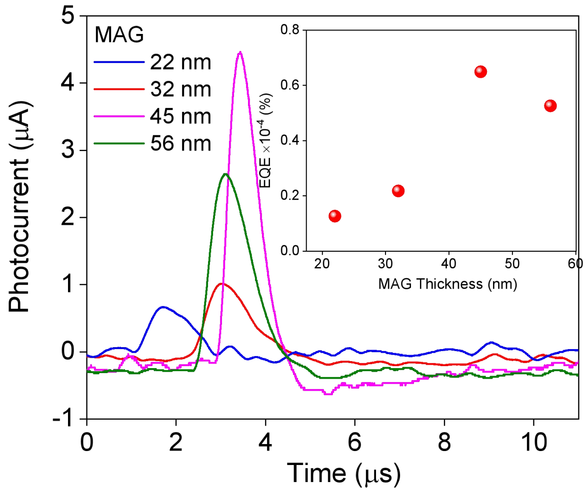

Figure S15 | Photocurrent and EQE of MAG/Si with different MAG thickness under 4 μm (10 mW mm^{-2}) laser illumination.

We explored the ultrafast transit photoresponse of the MAG/silicon to identify the mechanisms controlling the ultrafast dynamics, giving rise to an electron thermalization process, in particular the role of charge-carriers multiplication for the photovoltage generation. The beams are focused by objective lenses with a spot size ranging from 0.4 ~ 1.2 mm in diameter. As the 1 - 10 μm is a relatively broad wavelength range, the photon energies $h\nu$ are quite different in this range (2 × 10^{-19} J to 2 × 10^{-20} J). To compare the photoresponse of MAG/Si and SLG/Si, the laser fluence and spot size should be considered to fix the photon number N_{ph}:

$$\mathrm{R} = \frac{I_{ph}}{P} = \frac{\frac{Q}{t}}{\frac{W}{t}} = \frac{N_e \times e}{\boldsymbol{N_{ph}} \times h\nu} \qquad (1)$$

We calculated the external-QE as a function of the laser fluence by extracting the number of photo-excited charge-carriers from the transit photovoltage signal over the corresponding photon number of each laser pulse. Fig. 3b exhibits noise-equivalent-power: $\mathrm{NEP} = \frac{S_I}{R}$ and the specific detectivity: $D^* = \frac{\sqrt{A\Delta f}}{NEP}$ in the 1 μm to 10 μm infrared range of MAG/Si[18]. The NEP is from 10^{-12} to 10^{-6} W Hz$^{-1/2}$ in the 1 μm to 10 μm wavelength range, while the corresponding D* is from

10^{11} to 10^{6} Jones. Higher sensitivity and lower noise might be achievable at low temperatures, achieving the mid-infrared single-photon detection. We remark that the detectable spectral range is determined by Fermi-Dirac distribution and SBH. The spectral sensitivity can be further enhanced to extend the response spectral range.

As the 45 nm thick MAG is equal to 135 layers of stacked graphene, the density-of-states (DoS) of these layers can be integrated with the portion of the Fermi-Dirac distribution f(E) higher than the SBH. Then by considering the injection efficiency $\eta_e = A(\lambda) \cdot F(\phi_B) \cdot P(d)$ between the MAG and silicon[19], the photo-excited charge-carrier: $n(E) = A(\lambda) \cdot F(\phi_B) \cdot P(d) \cdot \mathrm{DoS(MGr)} \cdot \mathrm{f(E)}$ is equivalent to the charge-carriers collected at the silicon part. In the 1.34-2 μm wavelength range, IQE gradually changes from super-linear to sub-linear trend as photon energy increases. The transition can be described by fitting photocurrent versus laser power data with a parameter γ in $I \sim P^{\gamma}$[20], where γ gradually changes from 2.42 to 0.45 (Fig. S10 e). This transition indicates the electron-transfer from MAG to silicon is dominated from PTI to IPE as the wavelength decreases (photon energy increases). There are fewer data points to fit the trends in 4.2-7 μm wavelength ranges due to the lack of existing optical attenuators available.

Furthermore, we fabricated the MAG/Si photodiode with five different silicon wafers: highly-N doped (10^{18} cm^{-3}), lightly-N doped (10^{15} cm^{-3}), intrinsic (10^{12} cm^{-3}), lightly-P doped (10^{15} cm^{-3}), and highly-P doped (10^{18} cm^{-3}). The resultant band bending upward and downward lead to either electron or hole dominated transport, with Schottky barrier height 0.3 eV or 0.8 eV, respectively. The corresponding SNR of these five MGr/Si photodiodes is shown in Fig. S10 f, where the barrier against the forward diffusion charge-carriers gives rise to an optimal value.

The multiplication gain is about 10^2 at all laser fluence, which is calculated through M = (I_{ph} – I_{dark})/I_{ug}, where I_{ph} is the photocurrent, I_{dark} is the dark current and I_{ug} is the photocurrent when M=1[17]. Photo-excited hot electrons jumping over the Schottky barrier provide the major current source to trigger the avalanche, thus suppressing excess noise[21]: $S(f) = 2eI_{ug}M^2F(M)$ amperes during the avalanche. The excess noise factor F (M) is:

$$F(M) = M[1 - (1 - k)(\frac{M - 1}{M})^2]$$

where the k is the ionization coefficient.

Nonetheless, the wavelength of spectral detection is limited by the laser source (wavelength and fluency), rather than the intrinsic limitation of our MAG/Si (NEP and D*), which is estimated at approximately 10^4 photons, suggesting a promising gain for the full spectrum detection in mid-infrared.

Supplementary Note 6. The transit absorption measurements of MAG/Si.

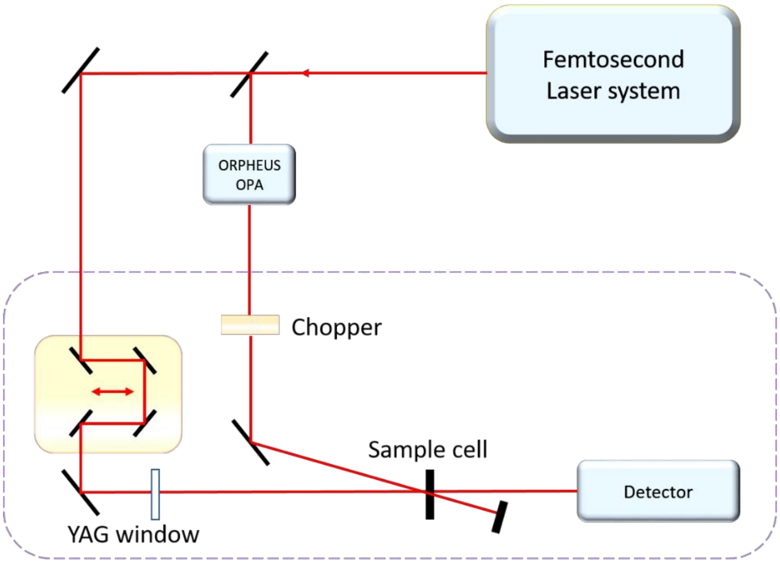

Figure S16 | The schematic of the transit absorption setup used in this work.

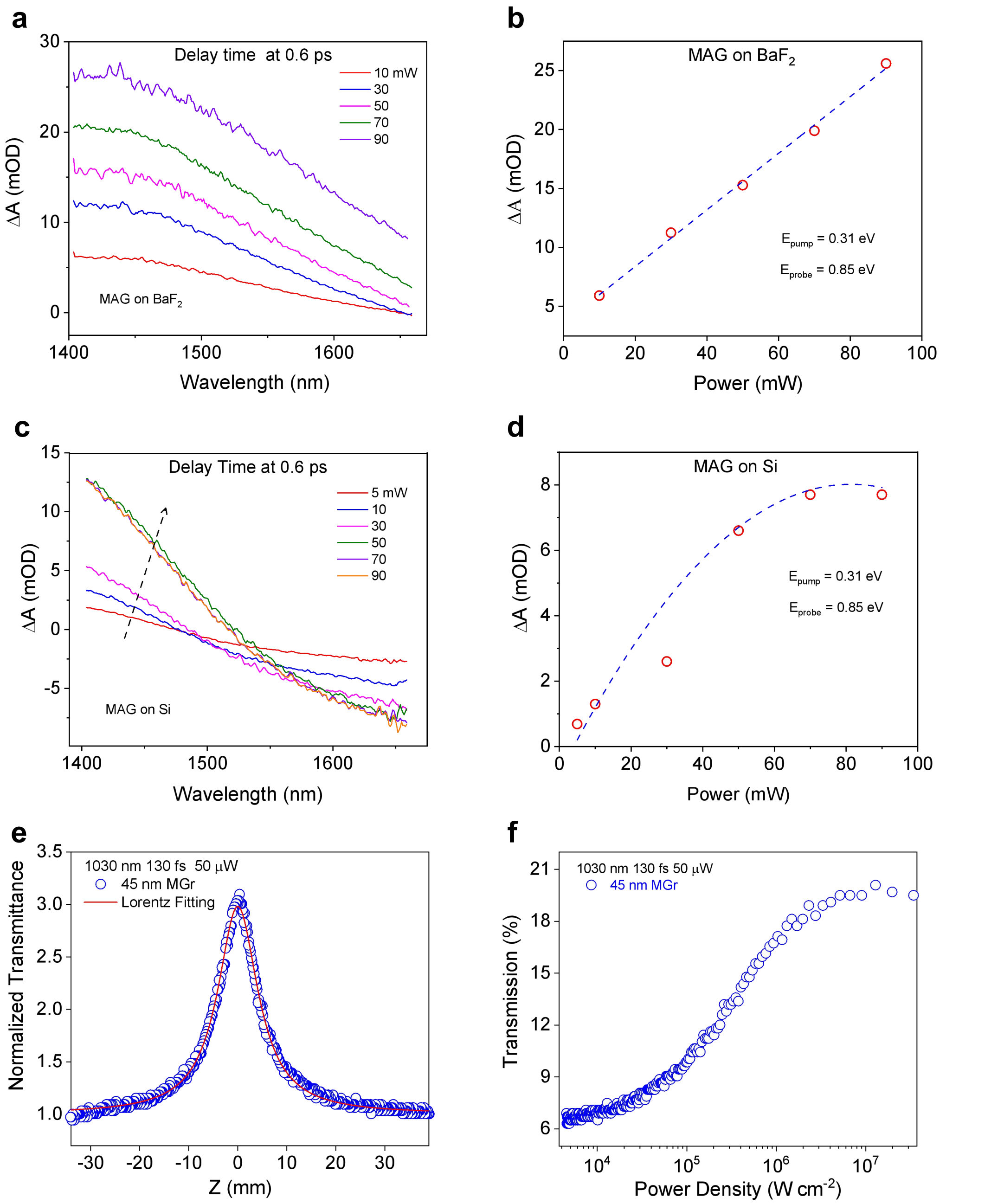

Figure S17 | The irradiance-dependent pump-probe studies. a-b, The transit-absorption of MAG on BaF_2 as a function of half of the probe laser photon energy under different laser irradiance at 0.6 ps delay time and its corresponding irradiance-dependent data. **c-d,** The transit-absorption of MAG on silicon as a function of half of the probe laser photon energy under different laser irradiance at 0.6 ps delay time and its corresponding irradiance-dependent data. **e-f,** The typical Z-scan data of MAG on BaF_2 recorded at 1300 nm and its corresponding input irradiance-dependent transmission.

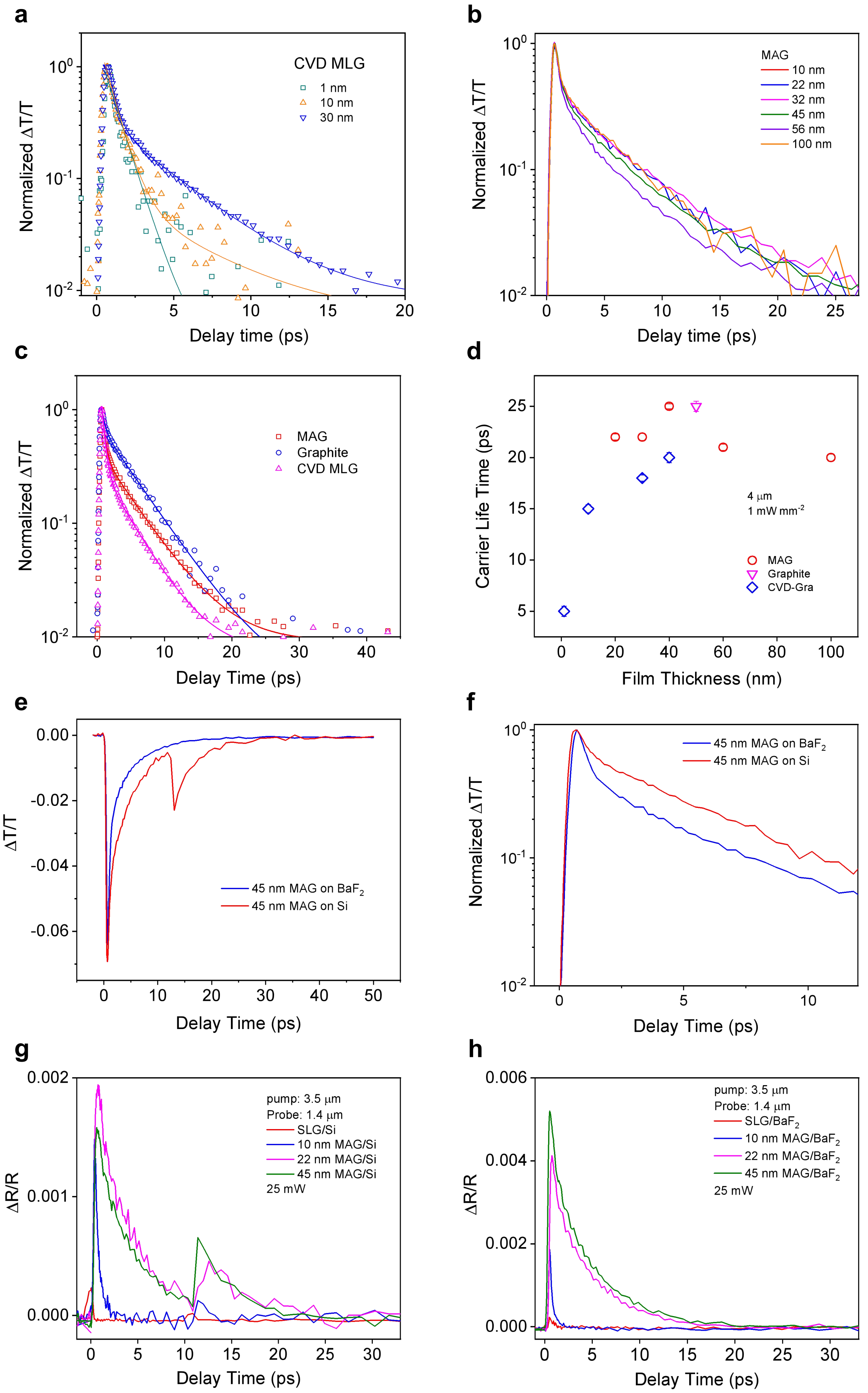

a
CVD MLG
1 nm
10 nm
30 nm
Normalized ΔT/T
Delay time (ps)
b
MAG
10 nm
22 nm
32 nm
45 nm
56 nm
100 nm
Normalized ΔT/T
Delay time (ps)
c
MAG
Graphite
CVD MLG
Normalized ΔT/T
Delay Time (ps)
d
4 μm
1 mW mm-2
MAG
Graphite
CVD-Gra
Carrier Life Time (ps)
Film Thickness (nm)
e
45 nm MAG on BaF2
45 nm MAG on Si
ΔT/T
Delay Time (ps)
f
45 nm MAG on BaF2
45 nm MAG on Si
Normalized ΔT/T
Delay Time (ps)
g
pump: 3.5 μm
Probe: 1.4 μm
SLG/Si
10 nm MAG/Si
22 nm MAG/Si
45 nm MAG/Si
25 mW
ΔR/R
Delay Time (ps)
h
pump: 3.5 μm
Probe: 1.4 μm
SLG/BaF2
10 nm MAG/BaF2
22 nm MAG/BaF2
45 nm MAG/BaF2
25 mW
ΔR/R
Delay Time (ps)

Figure S18 | The pump-probe studies. a-b, The normalized differential transmissivity of CVD-MLG and MAG with different thicknesses. **c,** The normalized differential transmissivity of the MAG, Graphite, and CVD-MLG with a thickness of 45 nm. **d,** The comparison of hot-carrier lifetimes in MAG, Graphite, and CVD-MLG as a function of film thickness. **e-f,** The differential transmissivity of MAG/BaF_2 and MAG/Si as a function of probe delay time. **g,** The normalized differential reflectance of SLG/Si, 22 nm MAG/Si, and 45 nm MAG/Si. **h,** The normalized differential reflectance of SLG/BaF_2, 22 nm MAG/BaF_2, and 45 nm MAG/BaF_2.

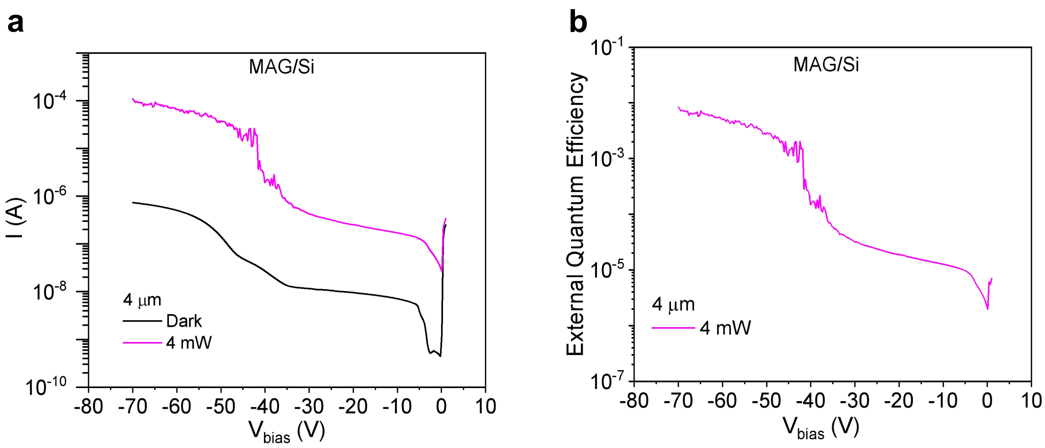

Figure S19 | Avalanche of MAG/Si. a-b, The dark *I-V* curves under 4 μm (4 mW mm^{-2}) laser illumination (**a**) and corresponding external-QE (**b**).

The differential reflectance $\frac{\Delta R}{R_0} = \left|\frac{R(n)-R_0}{R_0}\right|$ i.e. normalized difference of reflectance of the probe with $(R(n))$ and without (R_0) photoexcited carriers. The transfer reflectivity of MAG on a transparent substrate (BaF_2) depicts the distribution of photoexcited carrier density in the conduction band. The hot e-relaxation time at the SBH is much longer (> 20 ps) than that of single and multilayer layer graphene systems, which also supports the absence of accelerated hot electron cooling mechanisms that are usually observed in defected or disordered single or multilayer graphene[22,23]. The observed electron relaxation time indicates that the photo-generated carriers are effectively decoupled from the crystal lattice for longer length scales and thus allow a large portion of hot electrons to reach the MAG/Si interface. This longer hot electron relaxation time persists in MAG even when placed on the n-Si substrate. High-quality interfaces between graphene layers, the absence of accelerated relaxation mechanisms and the weak hot electron/ acoustic phonon coupling in the MIR range could lead to the observed large relaxation times in MAG. However, this higher hot electron density may not reflect in higher quantum yield due to various carrier recombination effects within MAG and at the MAG-Si interface. For instance, based on the previous studies on reduced graphene oxide samples[24], we can estimate the hot e-diffusion coefficient in MAG is ~ 1 $cm^2\ s^{-1}$ using Einstein relation for the hall mobility of MAG, ~ $10^3\ cm^2\ V^{-1}\ s^{-1}$ with the carrier temperature in the order of 1000 K. This indicates that the hot electrons confine in the in-plane geometry and thus mainly transport in out-of-plane geometry towards MAG-Si interface.

From the saturation absorption and power-dependent analysis, the two-photon or multi-photon absorption from either MAG or silicon, that may contribute to the photoresponse in our case, are ruled out (Fig. S17). The nonlinear light absorption of the MAG/Si sample was detected by using both transient absorption and Z-scan techniques. For all the Z-scan measurements, the maximum on-axis irradiance of the laser pulses was 150 mW mm^{-2} or lower at the focus. No laser-induced damage was observed in this irradiance range. The two-photon absorption contribution to the overall nonlinear signal was analyzed with the total absorption: $A = \frac{\alpha_0}{(1+\frac{I}{I_S})} + \beta I$, where the first term is the absorption saturation (α_0 is one-photon absorption coefficient and I_S is the saturation irradiance), and the second term quantifies the two-photon absorption (β is two-photon absorption coefficient and I is the laser irradiance). Fig. S17e-f indicates that the signals are dominated by saturable absorption due to Pauli blocking resulting from one-photon absorption. The two-photon absorption is too small to outperform the saturation of one-photon absorption. Though the excitation level could be up to 150 mW mm^{-2}, our analysis is limited to the range from a few to 10 mW mm^{-2}, avoiding the saturation absorption and other high-order nonlinear mechanisms (such as multi-photon absorption).

As shown in Fig. S18g-h, the differential reflectance ΔR/R of MAG/BaF_2, MAG/Si are two orders higher than those of SLG/BaF_2 and SLG/Si. Fig. 4 exhibits the hot-carrier multiplication in MAG at different pumping fluence as a function of delay time. In the vicinity of the charge neutrality point, interband heating takes place, leading to a larger free carrier density available for intraband heating. To be specific, the ratio of the photo-carrier number at the time *t* over that at 200 fs (the pump pulse width). Fig. 4 shows the photo-carriers density in the order of 10^8 cm^{-3} to the "hot-scattering" corresponding quasi-fermi level, in the employed pump-probe condition, where the dynamic SBH is also depicted. Nonetheless, we infer mobility of ~1000 cm^2 Vs^{-1} by combining the transport measurements with Hall measurements to extract the equilibrium DC conductivity 10^{-2} Ω^{-1} and the carrier density 10^{20} cm^{-3}. The hot-carrier-multiplication factor is calculated by $n_{(t > 200fs)}/n_{(200fs)}$: the hot-electron density (electrons with energy above the chemical potential) $n_{(t)}$ exceeding the electron density in the conduction band immediately after photo-excitation $n_{(200fs)}$.

Supplementary Note 5. The imaging method with MAG/Si.

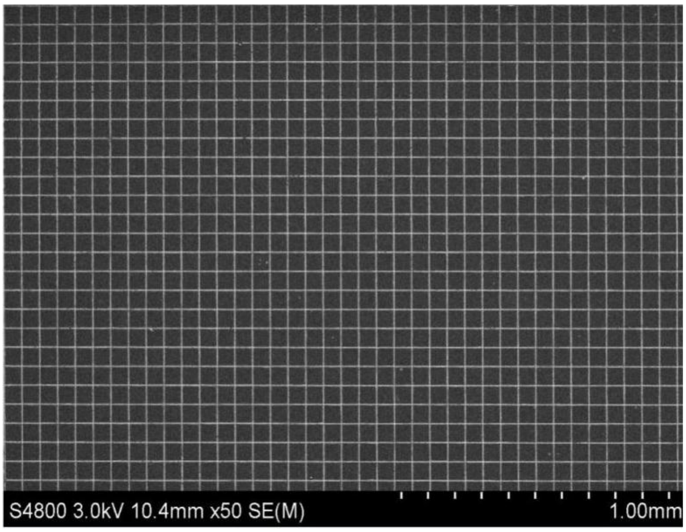

Figure S20 | The SEM image shows the oxygen plasma etched MAG pixel array on a silicon wafer.

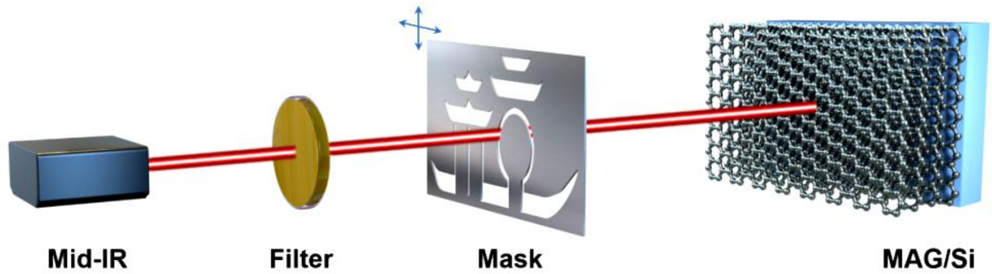

Figure S21 | The schematic of the imaging method. Infrared bandpass filters (FB2000-500 to FB4000-500, Thorlabs) were used to filter out the stray light from the MIR laser. A calcium fluoride aspherical lens was used to focus the infrared light on the device. A scanning system was built with a programmable X-Y stage. A data acquisition (DAQ) card was used to obtain the photocurrent data.

1 Cançado, L. G. *et al.* Measuring the degree of stacking order in graphite by Raman spectroscopy. *Carbon* **46**, 272-275 (2008).
2 Balandin, A. A. Low-frequency 1/f noise in graphene devices. *Nat. Nanotechnol.* **8**, 549-555 (2013).
3 Di Bartolomeo, A. Graphene Schottky diodes: An experimental review of the rectifying graphene/semiconductor heterojunction. *Physics Reports* **606**, 1-58 (2016).
4 Nair, R. R. *et al.* Fine structure constant defines visual transparency of graphene. *Science* **320**, 1308-1308 (2008).
5 Liu, X. *et al.* Infrared photodetector based on the photothermionic effect of graphene-nanowall/silicon heterojunction. *ACS Appl. Mater. Interfaces* **11**, 17663-17669 (2019).
6 Casalino, M. *et al.* Free-space Schottky graphene/silicon photodetectors operating at 2 μm. *ACS Photonics* **5**, 4577-4585 (2018).
7 Du, S. *et al.* Graphene/silicon-quantum-dots/Si Schottky-PN cascade heterojunction for short-wavelength infrared photodetection. *2017 IEEE International Electron Devices Meeting (IEDM)* 8.7.1-8.7.4 (2017).
8 Li, J. *et al.* Direct integration of polycrystalline graphene on silicon as a photodetector via plasma-assisted chemical vapor deposition. *J. Mater. Chem. C* **6**, 9682-9690 (2018).
9 Maurizio Casalino, Giuseppe Coppola, Mario Iodice, Ivo Rendina & Sirleto, L. Critically coupled silicon Fabry-Perot photodetectors based on the internal photoemission effect at 1550 nm. *Opt. Express* **20**, 12599–12609 (2012).
10 Maurizio Casalino *et al.* Cavity enhanced internal photoemission effect in silicon photodiode for sub-bandgap detection. *J. Lightwave Technol.* **28**, 3266-3272 (2010).
11 Casalino, M. *et al.* Vertically illuminated, resonant cavity enhanced, graphene–silicon Schottky photodetectors. *ACS Nano* **11**, 10955-10963 (2017).
12 Zhu, S., Yu, M. B., Lo, G. Q. & Kwong, D. L. Near-infrared waveguide-based nickel silicide Schottky-barrier photodetector for optical communications. *Appl. Phys. Lett.* **92**, 081103 (2008).
13 Casalino, M. *et al.* Cu/p-Si Schottky barrier-based near infrared photodetector integrated with a silicon-on-insulator waveguide. *Appl. Phys. Lett.* **96**, 241112 (2010).
14 Chen, Z. *et al.* Synergistic effects of plasmonics and electron trapping in graphene short-wave infrared photodetectors with ultrahigh responsivity. *ACS Nano* **11**, 430-437 (2017).
15 M. Casalino, M. Iodice, L. Sirleto, I. Rendina & Coppola, G. Asymmetric MSM sub-bandgap all-silicon photodetector with low dark current. *Opt. Express* **21**, 28072–28082 (2013).
16 Zhu, S., Chu, H. S., Lo, G. Q., Bai, P. & Kwong, D. L. Waveguide-integrated near-infrared detector with self-assembled metal silicide nanoparticles embedded in a silicon p-n junction. *Appl. Phys. Lett.* **100**, 061109 (2012).
17 Gao, A. *et al.* Observation of ballistic avalanche phenomena in nanoscale vertical InSe/BP heterostructures. *Nat. Nanotechnol.* **14**, 217-222 (2019).
18 Konstantatos, G. & Sargent, E. H. Nanostructured materials for photon detection. *Nat. Nanotechnol.* **5**, 391-400 (2010).
19 Casalino, M. Internal photoemission theory: comments and theoretical limitations on the performance of near-infrared silicon Schottky photodetectors. *IEEE J. Quantum Electron.* **52**,

1-10 (2016).

20 Ma, Q. *et al.* Tuning ultrafast electron thermalization pathways in a van der Waals heterostructure. *Nat. Phys.* **12**, 455-460 (2016).

21 Mcintyre, R.J. Multiplication noise in uniform avalanche diodes. *IEEE Trans. Electron Devices* 13,164-168(1966).

22 Graham, M. W., Shi, S.-F., Ralph, D. C., Park, J. & McEuen, P. L. Photocurrent measurements of supercollision cooling in graphene. *Nat. Phys.* **9**, 103-108 (2013).

23 Stange, A. *et al.* Hot electron cooling in graphite: Supercollision versus hot phonon decay. *Phys. Rev. B* **92**, 184303 (2015).

24 Ruzicka, B. A. *et al.* Hot carrier diffusion in graphene. *Phys. Rev. B* **82**, 195414 (2010).